Active disturbance rejection control system for rotary tiller tillage depth based on an improved snake optimizer

Wei Tao[1,2], Bin Chen[1,2*], Yihan Huang[1], Ruixin Li[1], Jiayi Ren[1], Xinkun Yang[1], Bo Guo[1], Jianjin Wu[1]

(1. *Fujian Provincial University Research Center for Digitalization and Intellectualization of the Bamboo Whole Industry Chain, Wuyi University, Nanping 354300, Fujian, China*;

2. *Fujian Key Laboratory of Big Data Application and Intellectualization for Tea Industry, Wuyi University, Nanping 354300, Fujian, China*)

Abstract: To address the challenge of low tillage depth precision in self-propelled electric rotary tillers operating under complex field conditions, this study proposes an active disturbance rejection control (ADRC) strategy with online parameter tuning realized by an improved snake optimizer (ISO). The ISO integrates three enhancement mechanisms—a multi-strategy chaotic system for population initialization, an anti-predator strategy for escaping local optima, and bidirectional population evolution dynamics for balancing exploration and exploitation. Sensor fusion of LiDAR terrain perception and displacement signals is accomplished through an extended Kalman filter, while a refined nonlinear function is embedded into both the extended state observer and the nonlinear state error feedback to strengthen disturbance estimation and compensation. Field experiments conducted in tea plantations at forward speeds of 0.72 and 1.20 km/h with target tillage depths of 50.00 and 90.00 mm show that the proposed ISO-ADRC system achieves a maximum depth deviation of 2.5 mm, an average standard deviation of 0.58 mm, and a coefficient of variation (CV) of (0.92±0.30)%. Compared with fuzzy PID, conventional ADRC, and IPSO-ADRC, the CV is reduced by 85.40%, 79.70%, and 20.00%, respectively. Simulation results further reveal a settling time of 0.102 s with zero overshoot and robust tracking performance under terrain disturbances. The proposed ISO-ADRC offers a compact electromechanical solution for precision tillage in tea plantation operations, serving as an effective alternative to conventional electro-hydraulic systems.

Keywords: electric rotary tiller, improved snake optimizer, active disturbance rejection control, tillage depth control

DOI: 10.25165/j.ijabe.20261902.9791

Citation: Tao W, Chen B, Huang Y H, Li R X, Ren J Y, Yang X K, et al. Active disturbance rejection control system for rotary tiller tillage depth based on an improved snake optimizer. Int J Agric & Biol Eng, 2026; 19(2): 203–214.

1 Introduction

Modern agricultural production increasingly relies on high-level mechanization to enhance operational efficiency and sustainability. Among various agricultural machinery, electric rotary tillers have gained prominence as key implements for seedbed preparation, with their performance directly affecting soil fragmentation, residue incorporation, and subsequent crop establishment[1,2]. One of the most critical factors governing tillage quality is the consistency of tillage depth, which significantly influences seed germination uniformity, root development, and overall yield potential[3]. Conventional tillage depth regulation methods, typically dependent on manual intervention or mechanical limit mechanisms, often suffer from inadequate precision, delayed response, and poor adaptability to varying field conditions, making them unsuitable for precision agriculture applications[4,5]. To overcome these limitations, modern electric rotary tillers are increasingly equipped with intelligent control systems capable of real-time monitoring and dynamic adjustment of tillage depth, thereby improving both work quality and operational efficiency in complex agricultural environments[6,7].

The challenge of precise tillage depth regulation has attracted considerable research attention, with numerous control strategies being explored. Hu et al.[8] developed an electro-hydraulic control system employing fuzzy adaptive PID (FAPID) to improve response speed and disturbance rejection in tillage depth stabilization. Similarly, Xiao et al.[9] implemented fuzzy PID control for a self-propelled electric tiller, utilizing resistance and angle sensors to achieve dual-parameter depth regulation. Gao et al.[10] proposed a variable universe fuzzy PID (VUFPID) controller that adapts to changes in tillage depth error and its derivative, demonstrating enhanced adaptability and anti-interference capabilities under variable field conditions. Wang et al.[11] introduced a hybrid extended state observer combined with back-stepping sliding mode control (HESO-Back Stepping SMC) to estimate unmeasured states and disturbances, achieving reliable performance in complex agricultural terrains. Tao et al.[12] presented a linear active disturbance rejection control (LADRC)-based system for electric rotary tillers, integrating posture sensor data to drive a hybrid stepper motor for precise depth regulation. Additional studies have explored improved fuzzy PID strategies, sliding mode adaptive control, and sliding mode control algorithms to address tillage depth control challenges[13-16]. Despite these advances, most existing approaches rely on traditional hydraulic actuation and have

Received date: 2025-08-19 **Accepted date:** 2026-03-29

Biographies: Wei Tao, PhD, Professor, research interest: optimal design of agricultural machinery and dynamic systems, Email: taowei@wuyiu.edu.cn; **Yihan Huang**, BS candidate, research interest: control system modeling and design, Email: 18359229772@163.com; **Ruixin Li**, BS candidate, research interest: control system testing and optimization, Email: 3167511366@qq.com; **Jiayi Ren**, BS candidate, research interest: agricultural robot control and navigation, Email: 3408854501@qq.com; **Xinkun Yang**, MS, Lecturer, research interest: autonomous navigation and control, Email: 71230538@qq.com; **Bo Guo**, MS, Professor, research interest: mechatronics design, Email: iamguobo@wuyiu.edu.cn; **Jianjin Wu**, BS candidate, research interest: electronic circuit design, Email: wujianjin20040206@163.com.

***Corresponding author: Bin Chen**, PhD, Professor, research interest: mechatronic system design and intelligent control for agricultural equipment. College of Mechanical and Electrical Engineering, Wuyi University, No. 358 Baihua Road, Wuyishan 354300, Fujian, China. Tel: +86-599-5136577, Email: binchen2009@gmail.com.

been primarily validated in conventional field settings, leaving gaps in the context of tea plantations, where narrow row spacing, undulating terrain, and high precision requirements demand more compact actuation and superior disturbance rejection capabilities.

Recent progress in intelligent control has highlighted the potential of metaheuristic optimization for controller parameter tuning. The snake optimizer (SO), introduced by Hashim and Hussien, is a bio-inspired algorithm that mimics the mating and foraging behaviors of snakes, offering strong global search capability and convergence properties[17]. However, the basic SO may encounter limitations in local exploitation during later iterations. To overcome this, various improved snake optimizer (ISO) variants have been developed. Zhi et al.[18] proposed an ISO incorporating chaotic elite opposition learning and sine-cosine search mechanisms, applying it to tune ADRC parameters for a rotary voice coil motor control system, achieving a scanning speed stability of 99.2%. Zhu et al.[19] developed a multi-strategy enhanced ISO featuring chaotic initialization, anti-predator exploration, and bidirectional population dynamics, which outperformed 120 benchmark functions and eight engineering optimization problems. Chetty et al.[20] employed SO for automatic voltage regulator tuning, leveraging its leader-follower mechanism to achieve superior transient response and disturbance rejection. Ersali et al.[21] introduced an opposition-based snake optimizer with pattern search (OSOPS) for PID-FF controller design in non-ideal buck converters, obtaining 14.21% and 32.10% faster rise times compared to SO and classical methods, respectively. These studies collectively confirm that ISO represents a powerful tool for addressing the parameter tuning challenges inherent in advanced control systems, yet its application to agricultural machinery control remains largely unexplored.

To address the identified gaps, this study proposes an ISO-ADRC-based real-time tillage depth control system for electric rotary tillers operating in tea plantation environments. The system integrates posture and displacement sensors via an extended Kalman filter to achieve accurate state estimation, while the ISO algorithm performs online optimization of ADRC observer and feedback gains. A hybrid stepper motor serves as the actuation unit, providing compact electromechanical control as an alternative to bulky hydraulic systems. The main contributions of this work are threefold:

1) An ISO-ADRC framework is established for real-time adaptive tuning of ADRC parameters, eliminating the need for empirical gain selection while improving optimization precision compared with conventional metaheuristics.

2) The proposed system represents the first application of ISO-ADRC to electric rotary tillers in tea plantation settings, addressing the unique challenges posed by narrow row spacing, irregular topography, and high tillage depth consistency requirements.

3) Comprehensive field experiments and simulations demonstrate significant improvements in tillage depth stability and dynamic response, with the coefficient of variation reduced by 83.7% relative to fuzzy PID and by 70.0% relative to LADRC, providing a robust and compact electromechanical solution for precision tillage operations.

2 Structural design of the rotary tiller body and control system

2.1 Structural design of the tiller body

As illustrated in Figure 1, the overall configuration of the electric rotary tiller comprises two main modules: a traveling unit and a working unit. The traveling unit constitutes the main chassis of the machine, while the working unit is mounted at the front end. The working unit integrates several key components, including rotary blades, synchronous pulleys, a reducer, a rotary tillage frame, a lead screw slide, an electric motor, and a blade shaft. A shaft-mounting hole is positioned at the lower section of the rotary tillage frame, with a diamond-shaped bearing seat installed to ensure stable support of the blade shaft. The rotary blades and a large synchronous pulley are mounted onto this shaft. The reducer is fixed on the upper platform of the frame, with its input end connected to the electric motor, while its output shaft carries a small synchronous pulley. This arrangement forms a two-stage reduction transmission system: the first-stage reduction is achieved through the reducer, followed by the second-stage reduction via a synchronous belt connecting the large and small pulleys. Such a design significantly amplifies output torque, thereby enhancing tillage efficiency under demanding soil conditions.

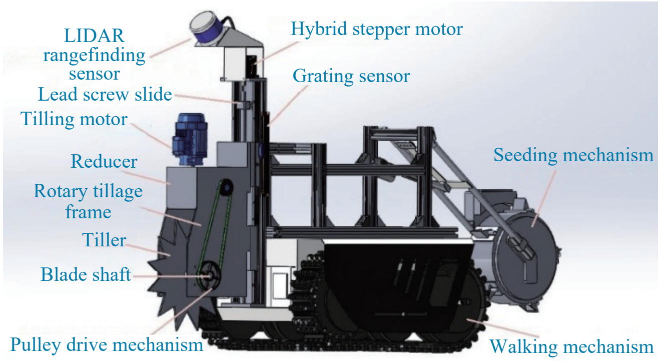

Figure 1 Overall structure of the electric rotary tiller

A connecting hole is provided at the rear of the frame, allowing it to be bolted to the lead screw slide. The slide table is coupled to a hybrid stepper motor via a coupling, enabling precise vertical positioning of the workbench through bidirectional motor rotation. This mechanism facilitates rapid and accurate adjustment of tillage depth. To further improve the system's adaptability to terrain variations, a laser radar (LiDAR) sensor is installed atop the hybrid stepper motor. This sensor performs real-time scanning of the ground surface ahead of the tiller, capturing terrain unevenness and transmitting the collected road surface profile information to the controller. By incorporating this pre-emptive terrain perception capability, the control system can proactively adjust tillage depth in response to incoming topographic changes, thereby enhancing depth consistency and reducing transient deviations induced by irregular ground surfaces.

2.2 Design of the adaptive real-time tillage depth control system

2.2.1 Control principle

The proposed adaptive real-time tillage depth control system comprises three principal modules: a LiDAR-based terrain perception unit, a central control unit, and a hybrid stepper motor-driven lead screw slide mechanism. Unlike conventional configurations that rely solely on posture sensing, the present system employs a LiDAR sensor mounted atop the stepper motor to capture ground surface undulations ahead of the rotary tiller. This forward-looking terrain perception enables proactive rather than reactive depth adjustments. The central control unit is built around an STM32F407 microcontroller, which integrates and processes incoming sensor data through an extended Kalman filter (EKF) to mitigate measurement noise and external disturbances such as vehicle vibration and attitude variation. The filtered signals are then fed into an ISO-ADRC (improved snake optimizer-based active disturbance rejection control) algorithm, which generates corresponding pulse control signals for the stepper motor driver. The lead screw slide, actuated by the stepper motor, governs the vertical displacement of the rotary tillage head. A grating sensor mounted on the guide rail provides real-time displacement feedback to the control unit, thereby closing the loop and enabling precise, adaptive tillage depth regulation. The overall workflow of the system is illustrated in Figure 2. The control algorithm execution cycle is 0.001 s (1 kHz sampling frequency).

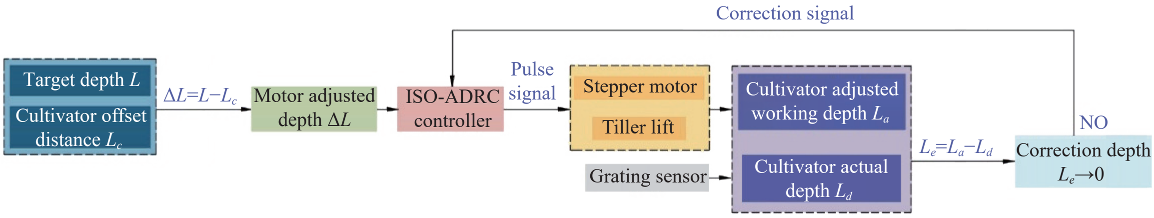

Figure 2 Workflow of the adaptive tillage-depth control system

The control process is executed in the following steps:

Step 1: Initial Depth Positioning

Upon receiving a remotely configured target tillage depth via wireless communication, the control unit calculates the required displacement and transmits corresponding pulse signals to the stepper motor. This drives the lead screw slide to lower the rotary tillage head to the preset depth. The grating sensor continuously monitors the actual displacement of the lead screw and provides real-time comparison feedback to ensure accurate initial positioning.

Step 2: Terrain-Adaptive Adjustment

During operation over uneven terrain, the LiDAR sensor scans the upcoming ground profile and relays the topographic information to the control unit. The microcontroller applies extended Kalman filtering to preprocess the LiDAR data, effectively attenuating high-frequency disturbances caused by machine vibration and transient attitude changes. Based on the estimated terrain irregularities, the ISO-ADRC controller computes the necessary compensation, converting it into pulse signals that command the stepper motor to adjust the height of the tillage head in real time, thereby maintaining the desired tillage depth despite varying ground conditions.

Step 3: Closed-Loop Depth Correction

Following each actuation, the grating sensor feeds back the measured displacement signal to the control unit as the actual tillage depth. The ISO-ADRC controller compares this measured value against the preset depth, adaptively correcting any deviation through its disturbance rejection and error compensation mechanisms. This closed-loop regulation ensures consistent tillage depth accuracy and stability throughout the entire operation.

2.2.2 Tillage depth variation model

The stepper motor operates as an open-loop actuation element, converting electrical pulse signals into discrete angular or linear displacements. The motor's rotational speed and stopping position are determined solely by the frequency and number of input pulse signals. Upon receiving each pulse, the stepper driver rotates the motor by a fixed step angle in the specified direction. The key operational parameters are governed by the following relationships:

$$\begin{cases} \theta = \dfrac{360}{N} \times K_0 \\ l = \dfrac{\theta \times \mathrm{P}}{360} \\ v = l \times 60 = f \times P \end{cases} \tag{1}$$

where, N denotes the step count of the stepper motor (dependent on the driver configuration); θ represents the motor rotation angle, (°); K_0 is the number of input pulses; l is the linear travel of the slide, mm; P is the lead screw pitch, mm; f is the pulse frequency, Hz; and v is the linear velocity of the slide, mm/s.

When the electric rotary tiller traverses uneven terrain, the tillage assembly experiences positional deviations that require compensatory actuation. The controller performs real-time adjustments to the stepper motor based on terrain irregularities detected by the LiDAR sensor, adaptively responding to tillage depth variations. The required adjustment is expressed as:

$$\Delta K = \frac{\Delta L \times N}{P} \tag{2}$$

where, ΔK denotes the number of variable pulses, and ΔL represents the corresponding tillage depth adjustment executed by the stepper motor. This value is derived from the terrain profile acquired by the LiDAR sensor, specifically from the vertical displacement of the blade tip and the height differential between the left and right tracks. Following actuation based on ΔK, the actual tillage depth is denoted as L_a, while the real-time depth measured by the grating scale sensor is recorded as L_d. The instantaneous depth control error can therefore be expressed as:

$$L_e = L_a - L_d \tag{3}$$

The tillage depth is dynamically corrected by the feedback controller, with L_e asymptotically converging to 0 within the minimum achievable time frame. This terrain-adaptive depth regulation methodology demonstrates superior performance in environments characterized by moderate topographic variations, such as tea plantations. The terrain roughness during tillage operations is continuously monitored by the LiDAR sensor mounted on the rotary tiller. As illustrated in Figure 3, let the horizontal mounting angle of the LiDAR sensor be α, with a vertical mounting height of h. The sensor returns distance measurements l_i $(i=1,2,3)$ corresponding to different forward scanning points. From these measurements, the depth variation z' immediately ahead of the blade tip can be derived based on geometric principles:

$$z' = l_1 \sin\alpha - h \tag{4}$$

Beyond the longitudinal depth variation induced by pitch angle dynamics, the tillage depth is also influenced by roll motion of the chassis. As depicted in Figure 3, the depth correction attributable to lateral roll variation is denoted as z'' and formulated as:

$$z'' = \frac{1}{2} \times (l_2 - l_3)\sin\alpha \tag{5}$$

By synthesizing Equations (4) and (5), the comprehensive real-time tillage depth adjustment ΔL can be obtained:

$$\Delta L = z' + z'' \tag{6}$$

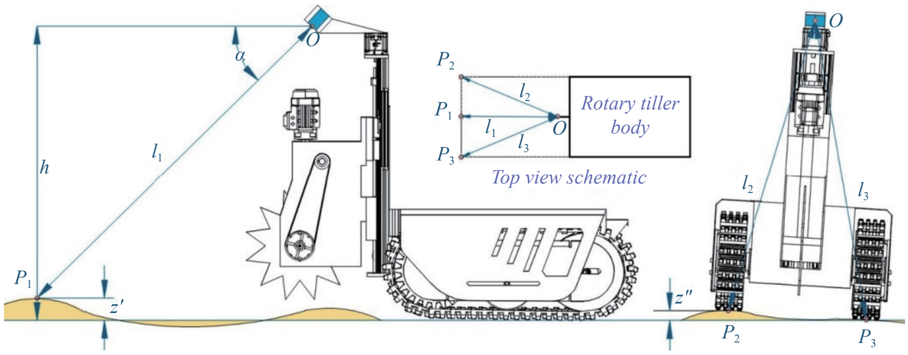

Figure 3 Geometric relationship between LiDAR terrain scanning and tillage depth variation

3 Real-time adaptive tillage depth control method

3.1 Automatic tillage depth control system and method

Conventional tillage depth regulation strategies can be broadly classified into position-based and force-based approaches, each exhibiting distinct advantages and limitations. Force-based adjustment remains insensitive to terrain undulations; however, real-time soil resistance measurement inaccuracies may compromise depth consistency. Conversely, position-based adjustment is unaffected by soil resistance variations but is susceptible to significant deviations under pronounced terrain fluctuations, necessitating supplementary sensing for error mitigation[22-24]. Two principal implementation paradigms exist for tillage depth control: mode switching and parameterized control coefficient methods. The latter, which relies on carefully calibrated control parameters, has been extensively investigated and has demonstrated superior control performance. Given the relatively moderate topographic variations characteristic of tea plantation environments, the parameterized control coefficient method is particularly advantageous for leveraging the benefits of position-based adjustment.

Following comprehensive consideration, the present study adopts a synergistic measurement architecture integrating a LiDAR sensor with a grating sensor, substantially attenuating the effects of vibration and external disturbances on the electric rotary tiller. The novel application of an ISO-ADRC (improved snake optimizer-based active disturbance rejection control) further minimizes tracking errors, while the hybrid stepper motor-driven mechanical configuration ensures stable and precise depth regulation. The LiDAR sensor serves as the primary terrain perception unit, continuously scanning the ground surface ahead of the tiller to capture topographic irregularities. After preprocessing via extended Kalman filtering to suppress measurement noise and transient disturbances, the desired tillage depth is compared against the actual depth to compute the required real-time adjustment. This adjustment signal is then processed by the ISO-ADRC controller and converted into pulse control commands for the stepper motor. The grating scale sensor provides real-time tillage depth feedback to the ISO-ADRC controller, thereby completing a closed-loop control architecture that enables adaptive real-time depth regulation.

3.2 Transfer function modeling of the hybrid stepper motor

The two-phase hybrid stepper motor employed in this study consists of stator and rotor assemblies fabricated from permanent magnet materials. The stator poles generate a magnetic field that interacts with the rotor poles to achieve synchronous rotation. The stator features eight uniformly distributed magnetic poles arranged into two-phase windings, with each phase containing four poles[25]. To facilitate mathematical modeling, the following factors are reasonably neglected:

1) Interpolar leakage flux in the stator
2) Permanent magnet leakage in the rotor
3) Hysteresis and eddy current losses
4) Harmonic components arising from stator coil self-inductance

A phase-equivalent mathematical representation is developed based on the electromagnetic circuit topology. When a pulse input θ_i is applied, the motor rotates to an actual angular displacement θ_o. The voltage balance equations for the two-phase hybrid stepper motor are expressed as,

$$\begin{cases} U_a = Ri_a + L\dfrac{\mathrm{d}i_a}{\mathrm{d}t} - K_m\omega\sin(Z_r\theta) \\ U_b = Ri_b + L\dfrac{\mathrm{d}i_b}{\mathrm{d}t} + K_m\omega\sin(Z_r\theta) \\ T_E = -K_m i_a\sin(Z_r\theta) + K_m i_b\cos(Z_r\theta) \end{cases} \tag{7}$$

where, U_a and U_b are the phase voltages, i_a and i_b are the corresponding phase currents, L denotes the average self-inductance, θ is the angular displacement, R is the phase resistance, J is the moment of inertia, B is the viscous damping coefficient, T_E is the electromagnetic torque, T_L is the load torque, Z_r is the number of rotor teeth, and K_m is the motor constant.

Under single-phase excitation with zero load torque, the dynamic behavior during motor energization can be derived from Equation (8).

$$J\frac{d^2\theta}{d^2t} + B\frac{\mathrm{d}\theta}{\mathrm{d}t} - \frac{Z_rLi_a^2}{2}\sin(Z_r\theta) = 0 \tag{8}$$

At the initial equilibrium state, the stepping-angle variation rate is approximately zero. The incremental motion equation is therefore:

$$J\frac{d^2(\Delta\theta)}{d^2t} + B\frac{\mathrm{d}(\Delta\theta)}{\mathrm{d}t} - \frac{Z_rLi_a^2}{2}\sin[Z_r(\Delta\theta)] = 0 \tag{9}$$

where, $\Delta\theta = \theta_o - \theta_i$. Given the infinitesimal magnitude of $\Delta\theta$, the small-angle approximation $\sin(Z_r\Delta\theta) \approx Z_r\Delta\theta$ linearizes Equation (9) to:

$$J\frac{d^2\theta_o}{d^2t} + B\frac{d\theta_o}{\mathrm{d}t} + \frac{Z_r^2Li_a^2}{2}\theta_o = \frac{Z_r^2Li_a^2}{2}\theta_i \tag{10}$$

Applying the Laplace transform under zero initial conditions yields:

$$\left(Js^2 + Bs + \frac{Z_r^2Li_a^2}{2}\right)\theta_o(s) = \frac{Z_r^2Li_a^2}{2}\theta_i(s) \tag{11}$$

The transfer function of the two-phase hybrid stepper motor is therefore expressed as,

$$G(s) = \frac{\theta_o(s)}{\theta_i(s)} = \frac{\dfrac{Z_r^2Li_a^2}{2J}}{s^2 + \dfrac{B}{J}s + \dfrac{Z_r^2Li_a^2}{2J}} \tag{12}$$

The parameters of the stepper motor utilized in this study (model JK86HS115-4208, manufactured by JKONG MOTOR Co., Ltd., Changzhou, China) are summarized in Table 1.

Table 1 Main parameters of the stepper motor

Parameter name	Parameter value
Number of rotor teeth Z_r	50
Phase current i_a/A	4.2
Viscous damping coefficient $\mathrm{N \cdot m \cdot s/rad}$	0.05
Moment of inertia $J/g{*}cm^2$	2700
Phase inductance L/mH	6.0

Substituting the aforementioned parameters into the transfer function given in Equation (12) yields:

$$G(s) = \frac{49.0}{s^2 + 0.0185s + 49.0} \tag{13}$$

3.3 Design of the ADRC controller architecture

ADRC, originally introduced by Han in 1998[26], is founded on the principle of treating all internal uncertainties and external disturbances as a lumped disturbance term, which is estimated and compensated in real time via an extended state observer (ESO). The ADRC framework comprises three essential components[27,28]:

- Tracking Differentiator (TD): Generates a smooth approximation of the reference input and its derivative, enabling rapid tracking without overshoot.
- Extended State Observer (ESO): Provides real-time estimation of both system states and the lumped disturbance, facilitating dynamic compensation for unmodeled dynamics and exogenous perturbations.
- Nonlinear State Error Feedback (NLSEF): Constructs the control law based on ESO outputs, achieving accurate state regulation through nonlinear error combination.

The fundamental architecture of ADRC is illustrated in Figure 4, where x denotes the reference input, d represents the total external disturbance, and y is the system output.

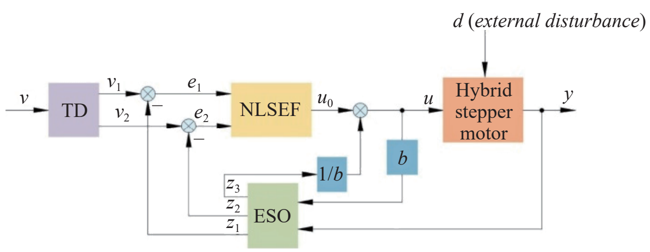

Figure 4 Basic structure of the ADRC framework

3.3.1 Tracking Differentiator

Within the ADRC framework, the TD achieves a smooth approximation of the generalized derivative of the input signal using nonlinear functions. The discrete-time formulation of a second-order TD algorithm is given by:

$$\begin{cases} v_1(k+1) = v_1(k) + Tv_2(k) \\ v_2(k+1) = v_2(k) + T\,\mathrm{fhan}(v_1(k) - x_0(k), v_2(k), r, \lambda_F) \end{cases} \tag{14}$$

where, T is the integration step size, r is the velocity factor, λ_F is the filtering coefficient, v_1 tracks the input x_0, v_2 approximates the derivative of v_1, and $\mathrm{fhan}(\cdot)$ is a nonlinear time-optimal synthesis function designed to suppress overshoot during transients. The piecewise definition of $\mathrm{fhan}(\cdot)$ is

$$\mathrm{fhan} = \begin{cases} d = rT;\ d_0 = \lambda_F d \\ y = v_1 - x_0 + Tv_2;\ a_0 = \sqrt{d^2 + 8r|y|} \\ a = \begin{cases} v_2 + \dfrac{y}{T},\ |y| \le d_0 \\ v_2 + \dfrac{a_0 - d}{2} sgn(y),\ |y| > d_0 \end{cases} \\ \mathrm{fhan} = \begin{cases} -r\dfrac{a}{d},\ |a| \le d \\ -rsgn(a),\ |a| > d \end{cases} \end{cases} \tag{15}$$

3.3.2 Extended State Observer with Improved Nonlinear Function

The ESO incorporates a nonlinear function to mitigate disturbance effects while maintaining stable regulation. Conventional ADRC implementations typically adopt the *fal* function as the fundamental nonlinear element, defined piecewise as,

$$fal(e,\alpha,\delta) = \begin{cases} |e|^{\alpha}\mathrm{sgn}(e),\ |e| > \delta \\ \dfrac{e}{\delta^{1-\alpha}},\ |e| \le \delta \end{cases} \tag{16}$$

where, e is the error signal, $\alpha \in (0,1)$ is the nonlinearity factor, and δ is the filtering coefficient. However, the conventional *fal* function exhibits an inflection point near the origin, leading to reduced smoothness. To address this limitation, this study introduces an optimized nonlinear function, denoted as *nfal*, formulated as,

$$nfal(e,\alpha,\delta) = \begin{cases} |e|^{\alpha}\left[\dfrac{2}{1+\exp(-\alpha e)} - 1\right],\ |e| > \delta \\ \dfrac{e}{\delta^{1-\alpha}},\ |e| \le \delta \end{cases} \tag{17}$$

Both *fal* and *nfal* are symmetric about the origin; however, *nfal* exhibits a smoother transition. In this study, the *nfal* function is employed to design the ADRC controller.

The ESO estimates unknown disturbances and unmodeled dynamics through compensatory feedback, enabling state reconstruction via real-time estimation. For a second-order system, the ESO can be expressed as,

$$\begin{cases} e = z_1 - \omega \\ \dot{z}_1 = z_2 - \beta_1 e + bu \\ \dot{z}_2 = -\beta_2 e \end{cases} \tag{18}$$

where, z_1 is the observed angular velocity of the stepper motor, z_2 is the total disturbance estimate, e is the observation error, and b is the compensation factor. For a second-order plant, a third-order ESO is required to estimate not only the two system states (position and velocity) but also the total disturbance, which includes internal uncertainties and external perturbations. This is a standard ADRC design[26].

To further enhance control performance, a third-order ESO is redesigned based on the *nfal* function, with its discrete-time algorithm given by:

$$\begin{cases} e = z_1(k) - y(k) \\ z_1(k+1) = z_1(k) + h_0[z_2(k) - \beta_{10}e] \\ z_2(k+1) = z_2(k) + h_0[z_3(k) - \beta_{20}nfal(e,\alpha_1,\delta) + bu] \\ z_3(k+1) = z_3(k) - h_0\beta_{30}nfal(e,\alpha_2,\delta) \end{cases} \tag{19}$$

where, z_1, z_2, and z_3 represent the state estimate, its derivative, and the total disturbance estimate, respectively; h_0 is the sampling step size; and β_{10}, β_{20}, β_{30} are tunable nonlinear gain coefficients.

Quantitative comparison shows that the *nfal*-based ESO reduces the integral absolute error (IAE) by 18.7% and the maximum disturbance estimation error by 22.4% compared with the traditional *fal* function under identical step and disturbance conditions.

3.3.3 Nonlinear State Error Feedback

The NLSEF constitutes a control law that is independent of the plant's mathematical model. Using the *nfal* function, the NLSEF algorithm is synthesized as,

$$\begin{cases} e_1 = v_1(k) - z_1(k) \\ e_2 = v_2(k) - z_2(k) \\ u_0 = \beta_1 nfal(e_1, \alpha_3, \delta_1) + \beta_2 nfal(e_2, \alpha_4, \delta_1) \\ u(k) = u_0 - z_3(k)/b \end{cases} \tag{20}$$

where, u_0 is the nonlinear compensation module combining proportional and derivative actions, and $z_3(k)/b$ is the disturbance compensation term that dynamically eliminates observed perturbations.

3.4 Design of the Improved Snake Optimizer (ISO)

3.4.1 Overview of the Baseline Snake Optimizer

The Snake Optimizer (SO), introduced by Hashim and Hussien in 2022, is a metaheuristic algorithm inspired by the natural behaviors of snakes, including foraging, combat, and mating[17]. Although SO represents a meaningful advancement over earlier optimization techniques, it exhibits notable limitations when applied to complex, high-dimensional engineering problems, particularly those involving multiple nonlinear constraints[29]. A key issue is its limited population diversity, which often leads to slow convergence, inadequate solution accuracy, and a pronounced tendency to become trapped in local optima—especially in search spaces with variable dimensions and strong nonlinearities[30]. To overcome these drawbacks, this paper proposes an Improved Snake Optimizer (ISO) that integrates three enhancement strategies: a Multi-Strategy Chaotic System (MSCS) for improving initialization and exploration, an Anti-Predator Strategy (APS) to escape local optima, and Bidirectional Population Evolution Dynamics (BPED) for balancing exploration and exploitation. A detailed flowchart of the proposed ISO is provided in Figure 5.

The ISO algorithm emulates the foraging and reproductive behaviors of snakes. The population of N candidate solutions (snakes) is evenly divided into male and female groups, as expressed in Equation (21).

$$\begin{cases} N_m \approx \dfrac{N}{2} \\ N_f = N - N_m \end{cases} \tag{21}$$

where, N is the total number of individuals, while N_m and N_f respectively denote the counts of male and female individuals.

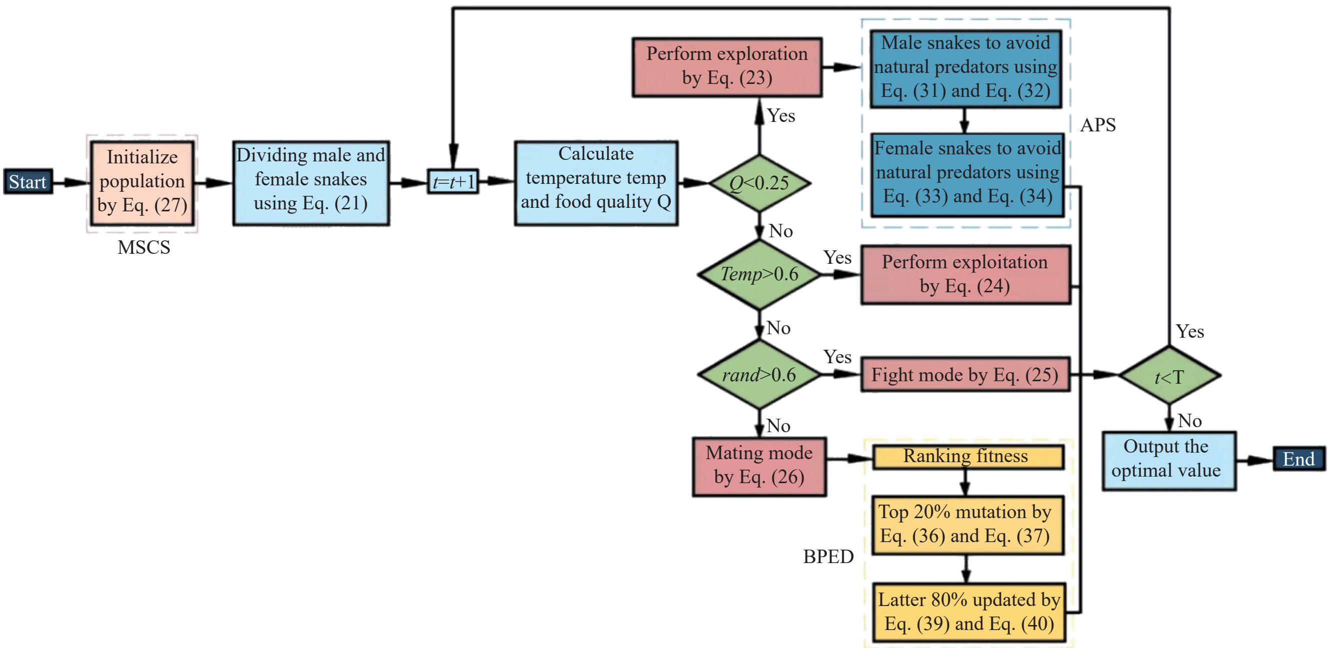

Figure 5 Flowchart of the proposed ISO algorithm

Combat or mating behaviors between females and males are initiated only when the temperature (Temp) is low and the food supply (Q) is abundant. The mathematical expressions for Temp and Q are given in Equation (22).

$$\begin{cases} Temp \approx \mathrm{e}^{\frac{-t}{T}} \\ Q = 0.5\mathrm{e}^{\frac{t-T}{T}} \end{cases} \tag{22}$$

where, T and t represent the maximum and current iteration counts, respectively.

The ISO algorithm also comprises two main phases: exploration and exploitation. When the food supply is scarce ($Q < 0.25$), the snakes enter the exploration phase and update their positions relative to the food source according to Equation (23).

$$X_{i,m}(t+1) = X_{\mathrm{rand},m}(t) \pm 0.05 \cdot \mathrm{e}^{\frac{-f_{\mathrm{rand},m}}{f_{i,m}}} \cdot ((X_{\max} - X_{\min}) \cdot \mathrm{rand} + X_{\min}) \tag{23}$$

where, $X_{i,m}$ and $X_{\mathrm{rand},m}$ represent the positions of male snakes, with their corresponding fitness values denoted as $f_{i,m}$ and $f_{\mathrm{rand},m}$, respectively; $X_{\max}$ and $X_{\min}$ denote the upper and lower bounds of the problem; and *rand* is a random number between 0 and 1. The position update method for female snakes follows the same formulation.

If food is available ($Q > 0.25$), the snakes enter the exploitation phase. Furthermore, if the temperature is greater than 0.6, they move directly toward the food source as described by Equation (24).

$$X_{i,j}(t+1) = X_{\mathrm{food}} \pm 2 \cdot Temp \cdot \mathrm{rand} \cdot (X_{\mathrm{food}} + X_{i,j}(t)) \tag{24}$$

where, $X_{i,j}$ and X_{food} represent the position of a snake (male or female) and the position of the best individual, respectively.

When the ambient temperature is low ($Temp < 0.6$), snakes enter either combat or mating mode. The combat mode for male snakes is described by Equation (25), while the mating mode is given by Equation (26).

$$X_{i,m}(t+1) = X_{i,m}(t) + 2\cdot e^{\frac{-f_{\text{best},f}}{f_i}} \cdot \text{rand} \cdot (Q \cdot X_{\text{best},f} - X_{i,m}(t)) \tag{25}$$

$$X_{i,m}(t+1) = X_{i,m}(t) + 2\cdot e^{\frac{-f_{i,f}}{f_{i,m}}} \cdot \text{rand} \cdot (Q \cdot X_{i,f}(t) - X_{i,m}(t)) \tag{26}$$

3.4.2 Multi-Strategy Chaotic System

The original SO algorithm employs a pseudorandom method to generate the initial population, which can lead to premature clustering of individuals and ultimately impair the algorithm's ability to balance local exploitation and global exploration. To enhance initialization performance, we introduce a Multi-Strategy Chaotic System (MSCS) for population initialization, drawing on chaos modeling techniques widely used in communication and information encryption. The mathematical formulation of the MSCS is given by Equation (27).

$$X_i = lb + F_{\text{MSCS}}(\delta, z_i)\cdot(ub - lb) \tag{27}$$

where, X_i denotes the i-th individual, and $F_{\text{MSCS}}(\delta, z_i)$ represents the Multi-Strategy Chaotic System. The variables ub and lb correspond to the upper and lower bounds of the problem, respectively. $F_{\text{MSCS}}(\delta, z_i)$ incorporates two distinct chaotic seeds: the chaotic seed $f_1(\mu, z_i)$, defined by the logistic chaotic map as shown in Equation (28), and the chaotic seed $f_2(a, z_i)$, given by the sinusoidal chaotic map as expressed in Equation (29). The MSCS ultimately outputs the result in the form of a sinusoidal transformation, thereby achieving complex and uniformly distributed chaotic behavior. The structure of the MSCS is presented in Equation (30).

$$\text{Logistic chaotic mapping}: z_{i+1} = f_1(\mu, z_i) = \mu z_i(1 - z_i) \tag{28}$$

$$\text{Sine chaotic mapping}: z_{i+1} = f_2(\alpha, z_i) = \frac{4}{\alpha}\sin(\pi z_i) \tag{29}$$

$$\text{MSCS}: z_{i+1} = F_{\text{MSCS}}(\delta, z_i) = |\sin(\pi(4\delta f_1(4, z_i) + (1-\delta) f_2(4, z_i)))| \tag{30}$$

where, $\mu \in [0,4]$ serves as the control parameter for the logistic chaotic map, while $a \in (0,4]$ is the control parameter for the sinusoidal chaotic map. In this study, we set $\mu = a = 4$ to construct the MSCS. Furthermore, $\delta \in [0,1]$ acts as the modulation parameter for the MSCS, and we select $\delta = 1$ in this work. Here, z denotes the current chaotic value within $[0,1]$, and z_{i+1} represents the output value of the MSCS.

3.4.3 Anti-Predator Strategy

In the SO algorithm, when food is unavailable, snakes enter the exploration or foraging phase. According to natural behavior, when snakes venture out for food, they may be attacked by natural predators. To cope with such threats, snakes attempt to evade predators and move away from their current location. We introduce an Anti-Predator Strategy (APS) into the SO algorithm to mathematically simulate this natural predator-avoidance behavior. The APS is activated only during the foraging phase when the food condition is poor ($Q < 0.25$). To enhance population diversity, male and female snakes adopt different predator-evasion strategies. The mathematical model of the APS for male snakes is given by Equations (31) and (32).

$$X_{m,i}(t) = X_i - \varphi\cdot(lb_i^{ap} + \text{rand}\cdot(ub_i^{ap} - lb_i^{ap})) \tag{31}$$

$$X_{m,i}(t+1) = \begin{cases} X_{m,i}, & \text{if } f_{m,i} < f_{i,m} \\ X_{i,m}, & \text{else} \end{cases} \tag{32}$$

where, $X_{m,i}(t)$ denotes the position of the i-th male snake in the presence of a predator. $\phi = [1 + F_{\text{MSCS}}(\delta, z_i) + 0.5] \in \{1,2\}$, meaning ϕ is a positive integer (either 1 or 2) randomly generated by the MSCS. $\text{rand} \in (0,1)$; $lb_i^{ap} = lb/t$, $ub_i^{ap} = ub/t$, where $t = 1,2,\ldots,T$. Here lb_i^{ap} and ub_i^{ap} represent the lower and upper bounds of the escape range for the snake when facing a predator. As the iteration proceeds, this range gradually shrinks, thereby accelerating convergence. $X_{i,m}$ indicates the position of a male snake during foraging in the exploration phase. $f_{m,i}$ and $f_{i,m}$ correspond to the fitness values of the male snake when adopting the anti-predator strategy and the predation strategy, respectively.

In nature, female snakes play a key role in population reproduction. Therefore, when under predatory threat, our objective is to better protect female snakes and guide them toward regions closer to superior samples. This behavior is modeled by Equations (33) and (34).

$$X_{f,i}(t) = X_i + \text{rand}\cdot(X_{\text{best},f} - \varphi X_i) \tag{33}$$

$$X_{f,i}(t+1) = \begin{cases} X_{f,i}, & \text{if } f_{f,i} < f_{i,f} \\ X_{i,f}, & \text{else} \end{cases} \tag{34}$$

where, $X_{f,i}(t)$ denotes the position of the i-th female snake in the presence of a predator, and $X_{\text{best},f}$ represents the best-known position of the female snake. $X_{i,f}$ indicates the position of a female snake while performing foraging behavior during the exploration phase; $f_{f,i}$ and $f_{i,f}$ correspond to the fitness values of the female snake when adopting the predator-avoidance strategy and the foraging strategy, respectively. If the new position of the snake is deemed safe, it is accepted; otherwise, the snake remains in its current location. This natural decision process is modeled by Equation (35).

$$X_i(t+1) = \begin{cases} X_{i+1}, & \text{if } f_{i+1} < f_i \\ X_i, & \text{else} \end{cases} \tag{35}$$

where, $X_i(t+1)$ denotes the position of the snake swarm, while f_{i+1} and f_i represent the fitness values of X_{i+1} and X_i, respectively.

3.4.4 Bidirectional Population Evolution Dynamics

The BPED strategy primarily consists of two steps. First, based on the widely observed Pareto principle in nature, the top 20% of individuals with favorable fitness are preserved through natural variation. For the high-quality population composed of these top 20% individuals, new mutated individuals $X_{\text{good,new}}$ are generated according to Equations (36) and (37).

$$X_{\text{good,new}}(t) = X_q + w\cdot(X_{\text{best}} - \varphi X_k) \tag{36}$$

$$X_{\text{good,new}}(t+1) = \begin{cases} X_{\text{good,new}}, & \text{if } f_{\text{good,new}} < f_i \\ X_i, & \text{else} \end{cases} \tag{37}$$

where, X_q and X_k represent two distinct high-quality individuals selected from the top 20% of the population, different from X_i; X_{best} denotes the most adapted individual within the top 20% ; and ψ is a mutation factor based on a sine function, whose specific expression is given by Equation (38).

$$\psi = \frac{\sin\left(\frac{2\pi t + \pi Dim}{Dim}\right)\cdot(t+T)}{2T} \tag{38}$$

where, Dim denotes the dimension of the problem, T the total number of iterations, and t the current iteration number.

The second part of the BPED strategy involves applying the PED strategy to mutate, eliminate, and migrate individuals in the remaining 80% of the population. This process generates new individuals, denoted as $X_{\mathrm{bad,new}}(t)$. The latter 80% of individuals are randomly divided into two groups. Those assigned to the first group undergo mutation around the best individual in the population. This process can be expressed by Equation (39).

$$X_{\mathrm{bad,new}}(t) = X_{\mathrm{best}} + sign(\mathrm{rand} - 0.5)\cdot(lb_i^{ap} + \mathrm{rand}\cdot(ub_i^{ap} - lb_i^{ap})) \quad (39)$$

A portion of the remaining 80% of individuals will undergo migration according to Equation (40), being relocated near their initial positions for further exploration:

$$X_{\mathrm{bad,new}}(t+1) = X_{\mathrm{bad,new}}(t) - 2\cdot sign(\mathrm{rand} - 0.5)\cdot(lb + \mathrm{rand}\cdot(ub - lb)) \quad (40)$$

Compared with the conventional PED strategy, the BPED strategy introduces a novel mutation approach that performs bidirectional operations on both high-performance and low-performance individuals. This raises the overall median fitness of the population and significantly enhances population diversity.

3.5 Integrated ISO-ADRC framework

3.5.1 Framework architecture and rationale

By synergizing the global optimization capability of ISO with the robust disturbance rejection of ADRC, an adaptive and high-performance control scheme is developed for the electric rotary tiller. This integration addresses a key challenge in precision tillage control: the automatic and optimal tuning of multiple controller parameters under complex, time-varying disturbances. ISO, with its enhanced search mechanisms, is uniquely positioned to navigate the high-dimensional, nonlinear parameter space of ADRC effectively.

The proposed architecture operates as a two-layer system, as illustrated in Figure 6:

1) Inner control loop: A fast, real-time loop where ADRC directly governs the hybrid stepper motor to regulate tillage depth and reject disturbances.

2) Outer optimization loop: A supervisory loop where the ISO metaheuristic optimizer dynamically adjusts the ADRC parameter vector θ to minimize a comprehensive tillage depth performance metric. This loop can operate in two modes:

○ Offline optimization: For initial controller calibration or benchmarking.

○ Online/adaptive optimization: Triggered by significant changes in terrain conditions or performance degradation, enabling real-time adaptation.

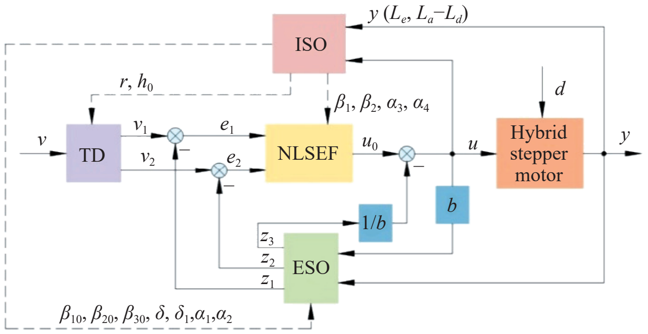

Figure 6 ISO-ADRC integrated control framework

This design decouples the tasks of robust stabilization (handled by ADRC) and performance optimization (handled by ISO), leading to a system that is both stable and perpetually self-optimizing for tillage depth accuracy.

3.5.2 ISO-driven ADRC parameter optimization

1) ADRC parameter vector

The vector θ encompasses the critical gains and parameters from all three ADRC modules:

$$\theta = [r, h_0, \omega_0, \beta_{10}, \beta_{20}, \beta_{30}, \beta_1, \beta_2, \alpha_1, \alpha_2, \alpha_3, \alpha_4, \delta, \delta_1] \quad (41)$$

where, r, h_0 are parameters for the Tracking Differentiator (TD); $\beta_{10}, \beta_{20}, \beta_{30}$ are nonlinear gain coefficients for the extended state observer (ESO); β_1, β_2 are gain coefficients for the nonlinear state error feedback (NLSEF); $\alpha_1, \alpha_2, \alpha_3, \alpha_4$ are nonlinearity factors for the *nfal* function; δ, δ_1 are filtering coefficients for the *nfal* function.

2) Performance metric (fitness function)

A composite fitness function $J(\theta)$ is defined to quantify tillage depth accuracy, system response, and control effort:

$$J(\theta) = \omega_1 \cdot \mathrm{RMS}(L_e) + \omega_2 \cdot \mathrm{RMS}(u) + \omega_3 \cdot \mathrm{RMS}(L_a - L_d) \quad (42)$$

where, L_e is tillage depth tracking error (primary accuracy indicator); u is control input to the stepper motor (energy consumption); $L_a - L_d$ is actual depth deviation after adjustment; $\omega_1, \omega_2, \omega_3$ are weighting coefficients.

Based on extensive simulation studies prioritizing tillage depth accuracy, the values $\omega_1 = 0.6$, $\omega_2 = 0.2$, and $\omega_3 = 0.2$ are adopted in this study.

3) Parameter constraints

To ensure controller stability and physical feasibility, each parameter in θ is bounded within a realistic range, as detailed in Table 2. The ISO algorithm incorporates a simple yet effective boundary handling mechanism: if a candidate solution exceeds a bound during iteration, the violating parameter is reset to its nearest bound. This maintains population feasibility without complex projections that might disrupt the algorithm's bio-inspired dynamics.

Table 2 Vector θ constraint range

Parameters	Meaning	Constraint Scope
r	Velocity factor	[10, 500]
h_0	Filtering factor	[0.001, 0.1]
$\beta_{10}, \beta_{20}, \beta_{30}$	ESO gains	[50, 500]
β_1, β_2	NLSEF gains	[0.1, 10]
$\alpha_1, \alpha_2, \alpha_3, \alpha_4$	Nonlinearity factors	[0.1, 0.9]
δ, δ_1	Filtering coefficients	[0.001, 0.1]

4) Optimization procedure

The ISO-driven optimization of ADRC parameters proceeds as follows:

Step 1 (Initialization): Generate the initial population of snake individuals using the MSCS strategy described in Section 3.5.2, with each individual representing a candidate parameter vector θ within the bounds defined in Table 2.

Step 2 (Fitness evaluation): For each candidate solution, simulate the closed-loop system response and compute the fitness value $J(\theta)$ according to Equation (42).

Step 3 (Population evolution): Update the population according to the ISO update rules (Equations (21)-(40)), including the exploration and exploitation phases, APS, and BPED strategies.

Step 4 (Convergence check): Repeat Steps 2 and 3 until the maximum iteration count is reached or the fitness improvement falls below a predefined threshold. The best-performing parameter vector θ^* is selected as the optimal ADRC configuration.

Step 5 (Real-time adaptation-optional): In online mode, a significant increase in measured tillage depth deviation (e.g., due to sudden terrain changes) can trigger a focused ISO re-optimization. Starting from the current θ^*, ISO performs a limited number of iterations to quickly find a better-adapted parameter set for the new condition.

The integrated ISO-ADRC framework thus presents a systematic, automated, and high-performance solution for electric rotary tiller depth control. It leverages ADRC's inherent robustness against disturbances and ISO's enhanced global search capability to find optimal control parameters that maximize tillage depth accuracy and consistency.

4 Simulation, field experiments, and results analysis

4.1 Simulation study of the adaptive tillage depth control system

To validate the proposed control strategy, a high-fidelity simulation model was developed in Simulink (MATLAB 2025) based on the adaptive tillage depth control methodology. The architectural schematic of the ISO-ADRC control system is illustrated in Figure 7, with critical design parameters enumerated in Table 3.

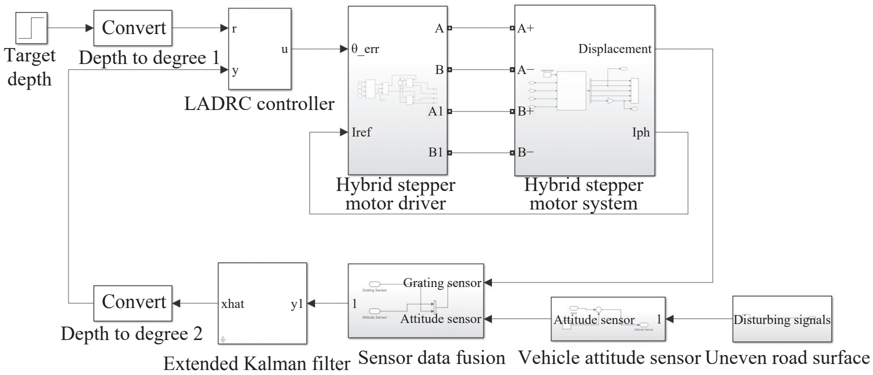

Figure 7 Simulation model of the ISO-ADRC control system

Table 3 Main design parameters of the ISO-ADRC controller

Module	Parameter	Symbol	Value
TD	Velocity factor	r	500
	Filtering coefficient	λ_F	0.01
	Integration step	T	0.0001
ESO	Sampling step	h_0	0.001
	Observer gain 1	β_{10}	0.05
	Observer gain 2	β_{20}	0.5
	Observer gain 3	β_{30}	30
	Nonlinearity factor 1	α_1	0.5
	Nonlinearity factor 2	α_2	0.5
	Filtering coefficient	δ	0.05
	Compensation factor	b	2
NLSEF	Nonlinearity factor 3	α_3	0.25
	Nonlinearity factor 4	α_4	0.25
	Gain coefficient 1	β_1	4000
	Gain coefficient 2	β_2	140
	Filtering coefficient	δ_1	0.05

In the simulation study, step response experiments were conducted under four control modes—conventional ADRC, fuzzy PID, IPSO-ADRC, and ISO-ADRC—with a preset tillage depth of 50 mm. The comparative step response characteristics are shown in Figure 8.

Figure 8 demonstrates that the ISO-ADRC controller exhibits superior rapidity compared with the other controllers. Specifically, the settling time is reduced by 25.5% relative to IPSO-ADRC and by 46.0% relative to conventional ADRC, while maintaining zero overshoot characteristics. The comparative results are quantitatively summarized in Table 4.

As shown in Figure 9, the ISO-ADRC controller demonstrates superior tracking performance in tillage depth control under simulated uneven terrain conditions with a preset value of 50 mm. Compared with fuzzy PID, ADRC, and IPSO-ADRC controllers, ISO-ADRC achieves significantly smaller dynamic tracking errors (e.g., 25.5% reduction in settling time relative to IPSO-ADRC) and maintains zero overshoot characteristics. Even under disturbances caused by road roughness and external perturbations, ISO-ADRC exhibits robust real-time control accuracy, with maximum depth deviations confined within ±1.8 mm.

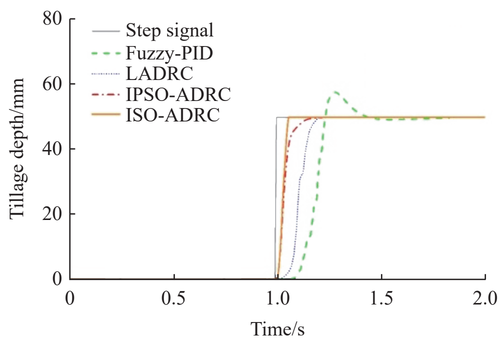

50 mm tillage depth step response

Figure 8 Step response plots for different tillage depth controllers

Table 4 Step response performance of different controllers at 50 mm target depth

Controller type	Settling time/s	Overshoot/%
ISO-ADRC	0.102	0
IPSO-ADRC	0.137	0
LADRC	0.189	0
Fuzzy PID	0.231	15.4

The simulated terrain disturbance consists of ±20 mm random undulations with a dominant frequency of 0.5 Hz, representing typical tea plantation roughness.

4.2 Experimental design

A comparative field study was conducted to evaluate the performance of four control systems (fuzzy PID, ADRC, IPSO-ADRC, and ISO-ADRC) for regulating the tillage depth of an electric rotary tiller under varying operational conditions. The field performance of these automated depth-control systems was systematically assessed, with emphasis on their ability to maintain agronomic requirements for depth uniformity and stability[12,31]. Key evaluation metrics included:

● Dynamic response characteristics: Settling time, overshoot, and steady-state error under terrain-induced disturbances (e.g., ±20 mm simulated soil undulations);

● Operational quality indices: Depth uniformity coefficient (CV≤8%, according to NY/T 740-2003 standards)[32].

As illustrated in Figure 10, the electric rotary tiller was specifically designed for tea–soybean intercropping systems in tea plantations. The experimental plot spanned 30 m in length, with the rotary blades operating at an average rotational speed of 150 r/min[33]. To address challenges associated with the lightweight design and limited power output of self-propelled electric tillers—where excessive rotational speeds combined with deeper tillage depths may induce blade slippage, incomplete soil fragmentation, and operational anomalies[34]—two operational speed levels (0.72 km/h and 1.2 km/h) were systematically evaluated.

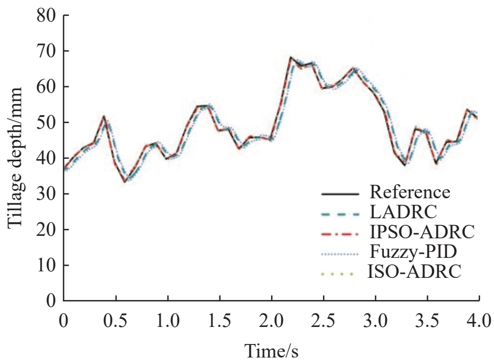

50 mm tillage depth disturbance signal response

Figure 9 Real-time control performance of different tillage depth controllers under disturbance signals

Figure 10 Experimental setup of the electric rotary tiller in field operation

Given the agronomic requirements for soybean cultivation (30-50 mm planting depth) and the need to ensure adequate soil preparation (50-100 mm tillage depth), predefined tillage depth settings of 50 mm and 90 mm were implemented under each speed condition. This resulted in four experimental combinations (Table 5), designed to quantify performance trade-offs between energy efficiency and soil processing quality.

Table 5 Test conditions for the field trials

Condition	Target tillage depth/mm	Working speed/km·h^{-1}
1	50	0.72
2	90	0.72
3	50	1.20
4	90	1.20

The tillage depth regulation system was evaluated under the four operational configurations listed in Table 5. A 20 m central zone was designated as the stabilized working area, with 5 m buffer segments at both ends to account for depth establishment transients. Each configuration underwent triplicate trials, with mean values calculated for statistical analysis. Comparative testing of the controllers was conducted through the following standardized procedure:

Step 1: System Calibration

Pre-trial verification included:

● Functional checks of control systems (CAN bus error rate < 0.1%);

● Validation of propulsion system torque output ((50±2) N·m via dynamometer);

● Blade rotational stability monitoring ((150±5) r/min through Hall-effect sensors).

Step 2: Control Algorithm Implementation

● ADRC Configuration: Initialized with conventional bandwidth parameters;

● IPSO-ADRC Configuration: Optimized parameters via improved particle swarm optimization;

● ISO-ADRC Configuration: Optimized parameters via the improved snake optimizer.

Step 3: Operational Execution

Upon timer initiation:

● Achieved target implement height within (3.2±0.5) s;

● Ground speed was maintained within the set value range using RTK-GNSS guidance.

Step 4: Spatial Sampling

Laser-scanned markers at 1 m intervals generated 20 measurement nodes.

Step 5: Post-Process Verification

Manual depth measurements were performed using a Vernier caliper at marked points, as shown in Figure 11.

Figure 11 Tillage depth data collection procedure

4.3 Experimental results and analysis

Experimental trials conducted under the four operational conditions (Table 5) demonstrated stable depth fluctuations within a controlled range throughout the tillage process. Variations in operational outcomes were observed due to differences in preset depth values and working speeds. As illustrated in Figure 12 and Table 6, the electric rotary tiller employing ISO-ADRC and IPSO-ADRC controllers achieved the target depth rapidly, while the conventional ADRC and fuzzy PID controllers exhibited comparatively inferior performance.

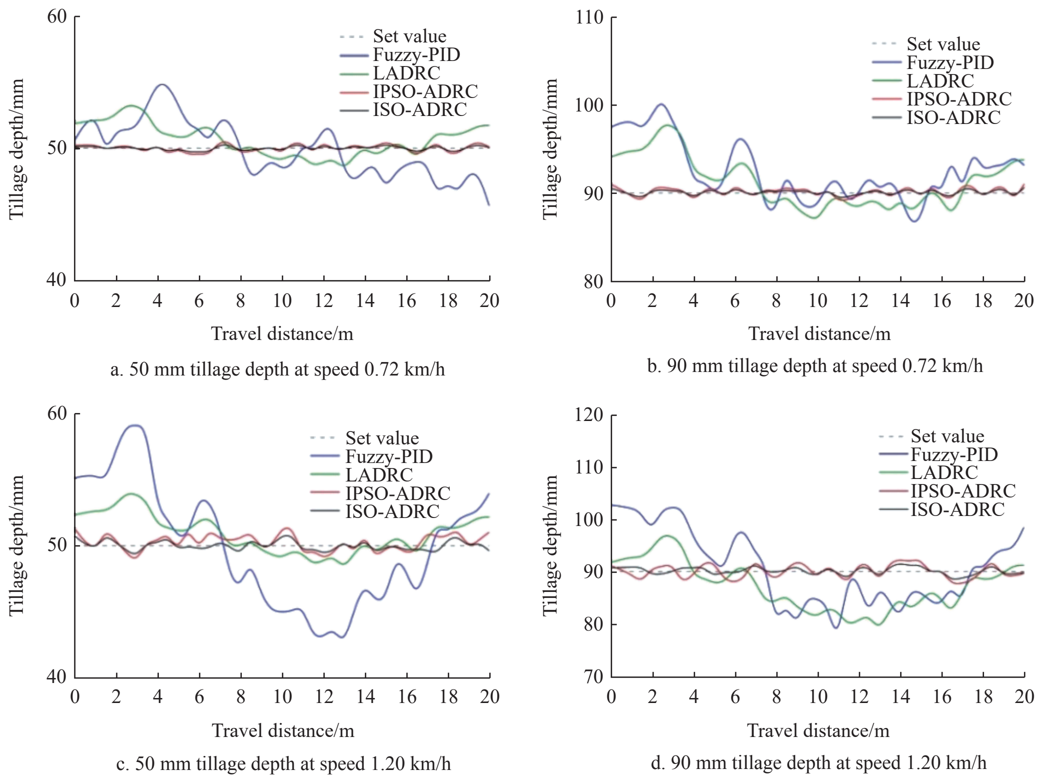

a. 50 mm tillage depth at speed 0.72 km/h

b. 90 mm tillage depth at speed 0.72 km/h

c. 50 mm tillage depth at speed 1.20 km/h

d. 90 mm tillage depth at speed 1.20 km/h

Figure 12 Rotary tillage depth under different control methods

Table 6 Summary of tillage depth control performance under different methods

Control method	Mean depth error/mm	Mean SD/mm	Mean CV/%	Group*
Fuzzy PID	3.85	4.62	6.28±1.80	a
ADRC	2.86	3.68	4.52±1.50	b
IPSO-ADRC	0.72	0.82	1.15±0.60	c
ISO-ADRC	0.42	0.58	0.92±0.30	d

Note: *Different letters indicate statistically significant differences between control methods (one-way ANOVA, $p<0.05$).

The ISO-ADRC control method maintained a maximum depth deviation of 2.5 mm and a minimum deviation of 0.5 mm across all conditions, with an average standard deviation of 0.58 mm and a stability CV of (0.92±0.3)%. Compared with IPSO-ADRC, ISO-ADRC reduced depth variability by 20.0%; compared with conventional ADRC, the reduction reached 79.7%; and relative to fuzzy PID, the reduction was 85.4%. One-way ANOVA further confirmed that the differences among the four controllers were statistically significant ($p<0.05$). These results confirm that the ISO-ADRC-controlled system significantly minimizes depth fluctuations and enhances operational stability under varying travel speeds, thereby improving tillage quality.

To further validate the performance differences among the four controllers, a one-way ANOVA was conducted on the coefficient of variation (CV) of tillage depth across all test conditions. The results (Table 6) showed a statistically significant difference among the four methods ($p=0.003<0.05$). Specifically, ISO-ADRC achieved the lowest CV (0.92±0.3)%, which was significantly lower than IPSO-ADRC (1.15±0.6)%, ADRC (4.52±1.5)%, and fuzzy PID (6.28±1.8)%. These results indicate that ISO-ADRC provides markedly superior stability in tillage depth control, effectively minimizing depth fluctuations under varying field conditions. The statistical analysis further confirms the robustness and reliability of the proposed ISO-ADRC approach compared with traditional and existing optimization-based controllers.

5 Conclusions

This study proposes an adaptive depth control system for electric rotary tillers, integrating LiDAR-based terrain perception, a hybrid stepper motor actuator, and an STM32 microcontroller. The core control strategy employs an ISO-ADRC framework, combining the global optimization of ISO with the disturbance rejection of ADRC for real-time, self-tuning tillage depth control. Simulation results show that the ISO-ADRC controller achieves a settling time of 0.102 s with zero overshoot, reducing settling time by 25.5% and 46.0% compared with IPSO-ADRC and conventional ADRC, respectively. Under terrain disturbances, depth deviations remain within ±3.0 mm. Field experiments under four operational conditions (target depths 50/90 mm, speeds 0.72/1.20 km/h) confirm the superiority of ISO-ADRC. The system achieves a maximum depth deviation of 2.5 mm, an average standard deviation of 0.58 mm, and a CV of (0.92±0.3)%. Compared with fuzzy PID, conventional ADRC, and IPSO-ADRC, ISO-ADRC reduces depth variability by 85.4%, 79.7%, and 20.0%, respectively. One-way ANOVA confirms statistically significant differences ($p=0.003$).

The closed-loop architecture, enabled by real-time grating sensor feedback and LiDAR terrain preview, ensures robust accuracy and adaptability. This work provides a compact electromechanical solution for precision tillage in tea plantations and offers insights for intelligent agricultural machinery development. Future work will explore multi-sensor fusion with machine learning-based terrain classification to further enhance adaptability.

Acknowledgements

This research was supported by the Natural Science Foundation of Fujian Province (Grant No. 2023J011041 and 2024J01909), the Fujian Provincial Key Science and Technology Project: Key Technologies and Equipment for Continuous and Intelligent Production of Bamboo Scrimber (Grant No. 2024HZ026011), the Nanping Science and Technology Plan Project (Grant No. N2023Z001, N2023Z002, and N2024Z001), the Nature Science Foundation of Nanping, China (Grant No. N2023J001, N2025J001, and N2025J002), and the Horizontal Projects of Wuyi University (Grant No. 2024-WHFW-030, 2025-WHFW-043, and 2026-WHFW-003).

[References]

[1] Fargnoli M, Parrella E, Costantino F, Tronci M. Hybrid solutions for agricultural vehicles: A comparative life cycle analysis from the users' standpoint. Journal of Cleaner Production, 2024; 485: 144406.

[2] Mousazadeh H, Keyhani A, Javadi A, Mobli H, Abrinia K, Sharifi A J E, et al. Life-cycle assessment of a solar assist plug-in hybrid electric tractor (SAPHT) in comparison with a conventional tractor. Energy Conversion Management, 2011; 52(3): 1700–1710.

[3] Fawzia H, Ahmeda D, Mostafac S A, Fudzeec M F M, Mahmoodd M A, Zeebareee S R, et al. A review of automated decision support techniques for improving tillage operations. REVISTA AUS, 2019; 26: 219–40.

[4] Jia H L, Guo M Z, Yu H B, Li Y, Feng X Z, Zhao J L, et al. An adaptable tillage depth monitoring system for tillage machine. Biosystems Engineering, 2016; 151: 187–199.

[5] Kim Y-S, Kim T-J, Kim Y-J, Lee S-D, Park S-U, Kim W-S. Development of a real-time tillage depth measurement system for agricultural tractors: application to the effect analysis of tillage depth on draft force during plow tillage. Sensors, 2020; 20(3): 912.

[6] Luo C H, Wen C K, Meng Z J, Liu H Y, Li G Q, Fu W Q, et al. Research on the slip rate control of a power shift tractor based on wheel speed and tillage depth adjustment. Agronomy, 2023; 13(2): 281.

[7] Romaneckas K, Steponavičius D, Jasinskas A, Kazlauskas M, Naujokienė V, Bručienė I, et al. How to analyze, detect and adjust variable seedbed depth in site-specific sowing systems: a case study. Agronomy, 2022; 12(5): 1092.

[8] Hu K, Zhang W Y, Qi B, Ji Y. Tillage depth dynamic monitoring and precise control system. Measurement Control, 2025; 58(3): 394–403.

[9] Xiao M H, Ma Y, Wang C, Chen J Y, Zhu Y J, Bartos P, et al. Design and experiment of fuzzy-PID based tillage depth control system for a self-propelled electric tiller. Int J Agric & Biol Eng, 2023; 16(4): 116–125.

[10] Gao Q, Lu Z X, Xue J L, Gao H S, Sar D. Fuzzy-PID controller with variable universe for tillage depth control on tractor-implement. Journal of Computational Methods in Science Engineering, 2021; 21(1): 19–29.

[11] Wang A Z, Ji X, Zhu Y Y, Wang Q Z, Wei X H, Zhang S C. Tillage depth regulation system via depth measurement feedback and composite sliding mode control: A field comparison validation study. Measurement Control, 2024; 57(6): 685–702.

[12] Tao W, Chen B, Yang X K, Guo B, Xu W W, Ke S Y, et al. Design and experimental study of tillage depth control system for electric rotary tiller based on LADRC. Scientific Reports, 2025; 15(1): 1740.

[13] Liu C Q, Gu J H, Xin D, Liu C W, Du Y F, Mao E R. Differential and integral sliding mode adaptive control algorithm for draft and position integrated control of electro-hydraulic hitch in agricultural tractor. INMATEH-Agricultural Engineering, 2023; 70(2): 369-378.

[14] Che Y C, Zheng G, Li Y, Hui X H, Li Y. Unmanned agricultural machine operation system in farmland based on improved fuzzy adaptive priority-driven control algorithm. Electronics, 2024; 13(20): 4141.

[15] Li M W, Xia X M, Zhu L T, Zhou R Y, Huang D Y. Intelligent sowing depth regulation system based on Flex sensor and Mamdani fuzzy model for a no-till planter. Int J Agric & Biol Eng, 2021; 14(6): 145–152.

[16] Sun X X, Song Y, Wang Y F, Qian J, Lu Z X, Wang T. Design and test of a tractor electro-hydraulic-suspension tillage-depth and loading-control system test bench. Agriculture, 2023; 13(10): 1884.

[17] Hashim F A, Hussien A G. Snake optimizer: A novel meta-heuristic optimization algorithm. Knowledge-Based Systems, 2022; 242: 108320.

[18] Zhi L J, Huang M, Qian L L, Wang Z C, Wen Q, Han W. Research on active disturbance rejection control with parameter autotuning for a moving mirror control system based on improved snake optimization. Electronics, 2024; 13(9): 1650.

[19] Zhu Y W, Huang H S, Wei J N, Yi J H, Liu J L, Li M M. ISO: An improved snake optimizer with multi-strategy enhancement for engineering optimization. Expert Systems with Applications, 2025; 281: 127660.

[20] Chetty N D, Gandhi R, Sharma G, Çelik E, Kumar R. Enhanced automatic voltage regulation using an extended PIDA controller optimised by the snake algorithm. Results in Engineering, 2025; 26: 105181.

[21] Ersali C, Hekimoglu B, Yilmaz M, Martinez-Morales A A, Akinci T C. Disturbance rejecting PID-FF controller design of a non-ideal buck converter using an innovative snake optimizer with pattern search algorithm. Heliyon, 2024; 10(14): e34448.

[22] Zhou L M, Ma Y H, Zhou H Y, Niu K, Zhao B, Wei L G, et al. Design and test of sowing depth measurement and control system for no-till corn seeder based on integrated electro-hydraulic drive. Applied Sciences, 2023; 13(10): 5823.

[23] Kim Y-S, Lee S-D, Baek S-M, Baek S-Y, Jeon H-H, Lee J-H, et al. Analysis of the effect of tillage depth on the working performance of tractor-moldboard plow system under various field environments. Sensors, 2022; 22(7): 2750.

[24] Zhang S L, Ren W, Xie B, Luo Z H, Wen C K, Chen Z J, et al. A combined control method of traction and ballast for an electric tractor in ploughing based on load transfer. Computers and Electronics in Agriculture, 2023; 207: 107750.

[25] Lai C-K, Lin B-W, Lai H-Y, Chen G-Y, editors. FPGA-based hybrid stepper motor drive system design by variable structure control. Actuators, 2021; 10: 113.

[26] Han J. From PID to active disturbance rejection control. IEEE Transactions on Industrial Electronics, 2009; 56(3): 900–906.

[27] Gao Z, Huang Y. Connecting theory and practice with ADRC. Control Theory and Technology, 2023; 21(1): 1–3.

[28] Jin H, Gao Z. On the notions of normality, locality, and operational stability in ADRC. Control Theory and Technology, 2023; 21(1): 97–109.

[29] Yao L G, Yuan P L, Tsai C-Y, Zhang T H, Lu Y, Ding S L. ESO: An enhanced snake optimizer for real-world engineering problems. Expert Systems with Applications, 2023; 230: 120594.

[30] Hu G, Yang R, Abbas M, Wei G. BEESO: multi-strategy boosted snake-inspired optimizer for engineering applications. Journal of Bionic Engineering, 2023; 20(4): 1791–827.

[31] Abduvakhobov D, Khabibullaev D K, Makhsudov A, Mukhammajonov K, Mirzaabdullayev M. A new method for determining the stability indicators of the depth of soil tillage. Научно-Технический Прогресс Как Механизм Развития Современного Общества, 2022; pp.81–84.

[32] NY/T 740-2003 standards. Technical specification for mechanized production in tea plantations. Beijing: Ministry of Agriculture of the People' s Republic of China, 2003.

[33] Zhong Y, Liang L, Xu R N, Xu H Y, Sun L, Liao H. Intercropping tea plantations with soybean and rapeseed enhances nitrogen fixation through shifts in soil microbial communities. Frontiers of Agricultural Science Engineering, 2022; 9(3): 344–355.

[34] Farzad M, Reza M M, Jalal K. Control of variable rate system of a rotary tiller based on real-time measurement of soil surface roughness. Soil Tillage Research, 2022; 215: 105216.